Large-Area and Visible-Light-Driven Heterojunctions of In_2O_3/Graphene Built for ppb-Level Formaldehyde Detection at Room Temperature

Guo, Lanpeng; Liang, Hongping; Hu, Huiyun; Shi, Shenbin; Wang, Chenxu; Li, Hao; Lee, Yi Kuen; French, Paddy J.; Wang, Yao; More Authors

DOI
10.1021/acsami.3c00218

Publication date
2023

Document Version
Final published version

Published in
ACS Applied Materials and Interfaces

ACS APPLIED MATERIALS & INTERFACES

www.acsami.org

Research Article

Large-Area and Visible-Light-Driven Heterojunctions of In_2O_3/Graphene Built for ppb-Level Formaldehyde Detection at Room Temperature

Lanpeng Guo, Hongping Liang, Huiyun Hu, Shenbin Shi, Chenxu Wang, Sitao Lv, Haihong Yang, Hao Li, Nicolaas Frans de Rooij, Yi-Kuen Lee, Paddy J. French, Yao Wang,* and Guofu Zhou

Cite This: *ACS Appl. Mater. Interfaces* 2023, 15, 18205−18216

Read Online

ACCESS | Metrics & More | Article Recommendations | Supporting Information

ABSTRACT: Achieving convenient and accurate detection of indoor ppb-level formaldehyde is an urgent requirement to ensure a healthy working and living environment for people. Herein, ultrasmall In_2O_3 nanorods and supramolecularly functionalized reduced graphene oxide are selected as hybrid components of visible-light-driven (VLD) heterojunctions to fabricate ppb-level formaldehyde (HCHO) gas sensors (named InAG sensors). Under 405 nm visible light illumination, the sensor exhibits an outstanding response toward ppb-level HCHO at room temperature, including the ultralow practical limit of detection (pLOD) of 5 ppb, high response (R_a/R_g = 2.4, 500 ppb), relatively short response/recovery time (119 s/179 s, 500 ppb), high selectivity, and long-term stability. The ultrasensitive room temperature HCHO-sensing property is derived from visible-light-driven and large-area heterojunctions between ultrasmall In_2O_3 nanorods and supramolecularly functionalized graphene nanosheets. The performance of the actual detection toward HCHO is evaluated in a 3 m^3 test chamber, confirming the practicability and reliability of the InAG sensor. This work provides an effective strategy for the development of low-power-consumption ppb-level gas sensors.

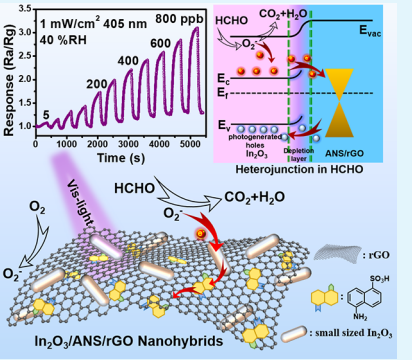

KEYWORDS: *In_2O_3 nanorods, supramolecularly functionalized graphene, formaldehyde sensing, room temperature, visible-light-driven heterojunctions*

INTRODUCTION

Formaldehyde (HCHO), one of the most toxic indoor pollutants, is widely derived from the volatilization of interior decoration materials such as furniture, paint, and wallpaper.[1] The recommended exposure limit (REL) for HCHO given by the World Health Organization (WHO) is 80 ppb.[2] Therefore, it is imperative to develop high-performance ppb-level HCHO monitoring sensors.

Conventional chemiresistive gas sensors based on metal oxide semiconductors (MOS) are one of the most intensively studied in the field of gas sensors.[3] However, high operating temperatures are required due to very few reactive oxygen species reacting with the gas on MOS's surface at room temperature (RT). Typically, the consequent problems of shortened lifetime, high power consumption, and poor safety further limit the application of MOS-based gas sensors.[4,5] Thus, room temperature detection of HCHO presents unique advantages owing to its low power consumption and wide safety margins. Light illumination is an important strategy for achieving RT sensing.[6,7] Li et al.[8] prepared Au-TiO_2 hollow nanospheres by the template method and achieved good detection of HCHO under 365 nm light. Despite these advances, the application of most MOS-based sensors is still limited due to their low sensitivity, relatively high practical limits of detection (pLOD), and poor selectivity. Precise detection of HCHO below 100 ppb at RT is still challenging and urgently needed.

To achieve better gas-sensing properties, hybridizing MOS and graphene nanosheets to form heterojunctions is considered an effective way.[9,10] Graphene has attracted much attention in the field of RT gas sensing owing to its atomically thick honeycomb lattice structure, high specific surface area, and excellent electrical conductivity.[11,12] In our previous work, we reported that the supramolecular assembly of a dipole (e.g., 5-aminonaphthalene-1-sulfonic acid, etc.) with reduced graphene oxide (rGO) can significantly promote its charge transfer rate.[13,14] Compared with other MOS, indium oxide (In_2O_3), as a typical n-type semiconductor with excellent optoelectronic properties, good thermal stability, low resis-

Received: January 6, 2023
Accepted: March 16, 2023
Published: March 31, 2023

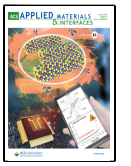

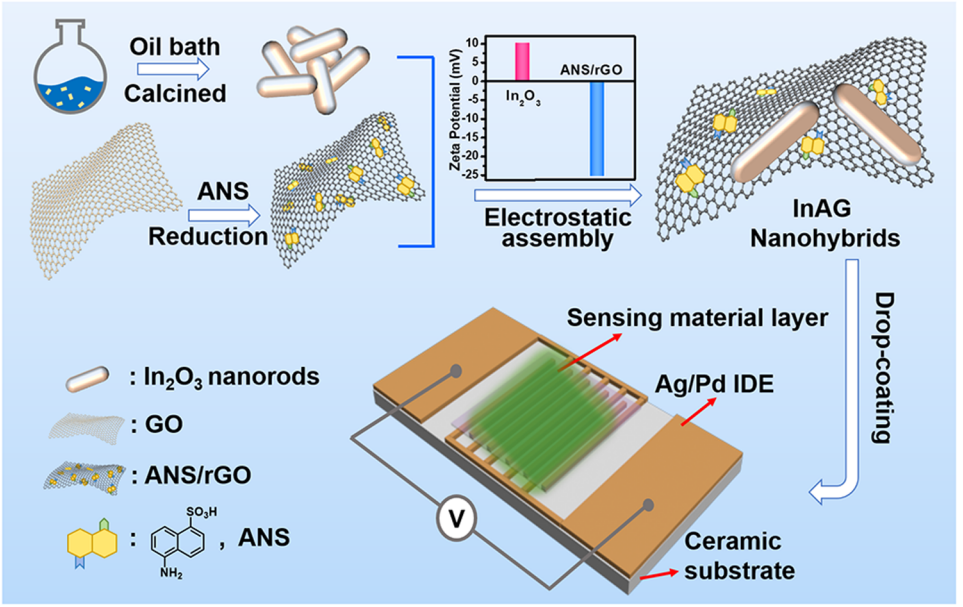

Figure 1. Schematic diagram of the preparation process of InAG nanohybrids and a gas sensor.

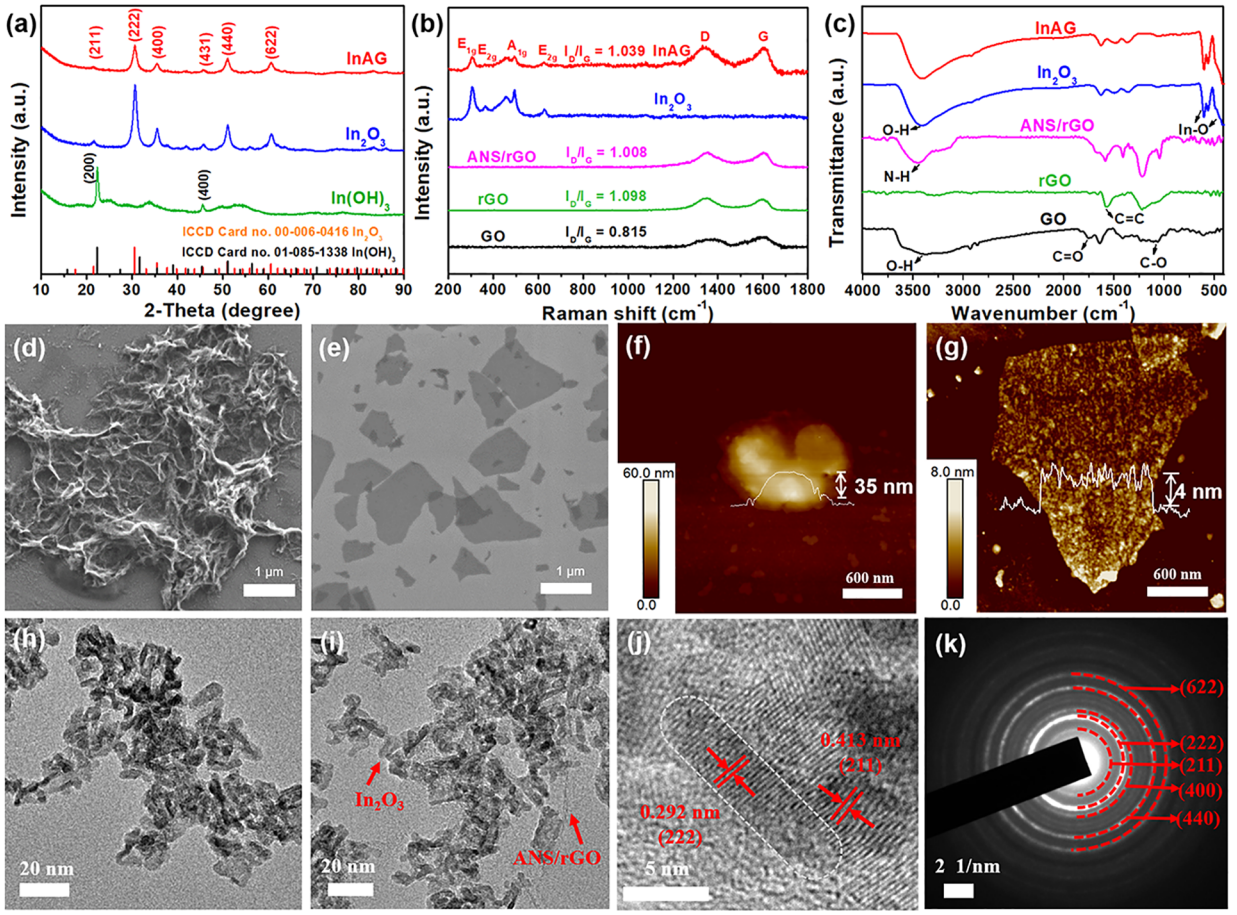

Figure 2. (a) XRD patterns of InAG nanohybrids, pristine In_2O_3 nanorods, and $In(OH)_3$. (b) Raman and (c) FTIR spectra of InAG, In_2O_3 nanorods, ANS/rGO, rGO, and GO nanosheets. SEM images of (d) rGO and (e) ANS/rGO nanosheets. AFM images and corresponding height profiles of (f) rGO and (g) ANS/rGO nanosheets. TEM images of (h) pristine In_2O_3 nanorods and (i) InAG nanohybrids. (j) HRTEM image and (k) SAED pattern of InAG nanohybrids.

tivity, and high catalytic activity, is regarded as one of the most promising HCHO-sensing materials.[15,16] Furthermore, In_2O_3 is easy to modulate for defects due to the nonstoichiometric phase structure and readily obtains a homogeneous morphol-

https://doi.org/10.1021/acsami.3c00218
ACS Appl. Mater. Interfaces 2023, 15, 18205−18216

ogy by liquid phase methods.[17,18] A recent study suggests that In_2O_3 containing defects has a strong adsorption capacity for HCHO,[5] which can effectively improve the selectivity without additional molecular filter membrane coverings,[19] etc. For the past few years, some works have demonstrated that In_2O_3/rGO composites exhibit high room temperature gas responsivity.[20,21] However, the relatively higher pLOD still limits their further application. To the best of our knowledge, no one has tried to combine In_2O_3 with rGO for room temperature HCHO sensing so far.

In general, the specific surface area of nanoparticles increases with the decrease of size.[22] Hence, it is believed that when small size nanoparticles are selected to assemble with graphene, a larger interfacial contact area and more heterojunctions of In_2O_3/rGO will be obtained, which should be beneficial to improve the gas-sensing properties. Therefore, the preparation of smaller In_2O_3 nanoparticles to assemble with 5-aminonaphthalene-1-sulfonic acid (ANS)-modified graphene nanosheets forming more interfaces of heterojunctions could be a good approach to verify the impact of heterojunctions on gas sensing.

In this work, inspired by the above speculations, we designed and prepared visible-light-driven (VLD) heterojunctions of InAG which was composed of functionalized graphene nanosheets and ultrasmall In_2O_3 nanorods with an average diameter of 3.2 nm which is lower than the Debye length. The corresponding InAG-based gas sensor was fabricated for ppb-level room temperature formaldehyde sensing. The InAG-based sensor exhibited outstanding HCHO-sensing properties under 405 nm illumination at room temperature and behaved with remarkable practicability and reliability in a 3 m^3 test chamber. The gas-sensing mechanism of InAG has been proposed based on the measurement with ultraviolet photoelectron spectroscopy (UPS) and the literature. It is illustrated that the generation of more interfacial depletion layers and the implementation of more efficient charge transfer are jointly responsible for the ultrasensitive room temperature HCHO-sensing properties of InAG.

RESULTS AND DISCUSSION

Synthesis and Sensor Fabrication. Figure 1 illustrates the process flow for the preparation of InAG nanohybrids and an RT gas sensor. To solve the problem of poor dispersibility of graphene, ANS molecules are attached to graphene through $\pi-\pi$ stacking supramolecular interactions. The negatively charged $-SO_3^-$ groups provide sufficient electrostatic repulsion to maintain excellent water dispersibility of ANS/rGO nanosheets (Figure S1). As shown in Figure 1, the ANS/rGO and the In_2O_3 show opposite charges, indicating that they can be easily assembled by electrostatic interaction.

Characterization of Gas-Sensing Materials. The crystal structures of the synthesized samples were determined by XRD analysis. As shown in Figure 2a, the diffraction peaks of the In_2O_3 nanorod precursor can be correlated with $In(OH)_3$ (ICDD card no. 01-085-1338). The highest-intensity diffraction peak corresponding to the (200) crystal plane indicates that $In(OH)_3$ grows along the [100] orientation.[9] According to ICDD card no. 00-006-0416, the diffraction peaks of calcined In_2O_3 nanorods at 2θ of 30.58°, 35.46°, 51.03°, and 57.55° match with the crystal faces of (222), (400), (440), and (622) of the cubic In_2O_3. After assembling with ANS/rGO nanosheets, the diffraction peaks of InAG nanohybrids presented as similar to those of the pure In_2O_3 nanorods. Furthermore, no characteristic diffraction peaks of carbon species are observed in the hybrids due to the relatively low content of ANS/rGO. As shown in Figure 2b, the reduction of GO and the presence of ANS/rGO in InAG nanohybrids are confirmed by Raman spectroscopy. In the spectrum of In_2O_3 nanorods, the Raman peaks at 306 cm^{-1} (E_{1g}), 363 cm^{-1} (E_{2g}), 492 cm^{-1} (A_{1g}), and 624 cm^{-1} (E_{2g}) correspond to the optical phonons associated with the cubic crystal structure of In_2O_3.[23] The peaks at 306 and 363 cm^{-1} are attributed to the bending vibration of the InO_6 octahedron [$\delta(InO_6)$] and the stretching vibration of the indium−oxygen−indium bond [υ(In—O—In)], respectively.[9,24] The peaks at 492 and 624 cm^{-1} are assigned to the stretching vibration of the InO_6 octahedron [$\upsilon(InO_6)$].[25] As expected, InAG displays two main D-band and G-band peaks at 1341 and 1599 cm^{-1}, respectively, confirming the successful assembly of In_2O_3 nanorods on ANS/rGO nanosheets. The D-band is related to structural defects in graphene, and the G-band is attributed to the first-order scattering of the E_{2g} mode of the sp^2 bonds of carbon atoms.[26] The peak intensity ratio of the D-band and G-band (I_D/I_G) is customarily used to evaluate the degree of disorder and defects in graphitic structure. The I_D/I_G values of rGO, ANS/rGO, and InAG are all higher than that of GO, which indicates that GO has been successfully reduced.[27] The FTIR spectra of the samples are shown in Figure 2c. In the spectrum of rGO, the characteristic absorption band at 1568 cm^{-1} is attributed to C=C skeleton vibration.[26] Moreover, the characteristic peaks of oxygen-containing groups in GO, including C—O (1050 cm^{-1}), C=O (1740 cm^{-1}), and O—H (3400 cm^{-1}),[26,28] are not found in rGO, indicating that graphene oxide is reduced. Compared with rGO, the broader peak at 3420 cm^{-1} of ANS/rGO can be attributed to N—H stretching vibration from the ANS molecule, confirming the successful assembly of rGO with the ANS molecule. For In_2O_3 nanorods and InAG nanohybrids, the well-identified vibrational bands around 420, 567, and 604 cm^{-1} can be attributed to In—O lattice vibrations of In_2O_3.[29] A broad peak corresponding to the O—H stretching vibration appeared at 3400 cm^{-1}, which may be related to the adsorbed water vapor and hydroxyl groups on the surface of In_2O_3 nanomaterials.[29]

The morphology and microstructure of the prepared samples were observed by SEM, AFM, and TEM. It can be seen from Figure 2d that rGO has an obvious stacking phenomenon. The height of the representative rGO measured by AFM in Figure 2f is 35 nm. In contrast, the morphology of the as-prepared ANS/rGO is typical of graphene sheets (Figure 2e), demonstrating that the supramolecular assembly of ANS molecules can prevent severe stacking between rGO sheets. The AFM height profile in Figure 2g shows that the ANS/rGO nanosheet has a thickness of 4 nm. Figure S2 exhibits the SEM images of In_2O_3 nanorods, InAG, In_2O_3 microrods, and InMAG. It can be seen from Figure S2a that the morphologies of the as-prepared In_2O_3 nanorods are tiny nanoparticles. For the InAG nanohybrids, In_2O_3 nanoparticles are embedded in the network composed of ANS/rGO nanosheets (Figure S2b), which proves that the anchoring of In_2O_3 on ANS/rGO nanosheets through electrostatic interaction is an effective strategy. Owing to the small size of In_2O_3 nanorods and the good dispersion of ANS/rGO nanosheets, large heterojunctions are formed at the interface, which is favorable for gas sensing. As a comparison, SEM images of In_2O_3 microrods and InMAG are shown in Figure S2c,d. The

https://doi.org/10.1021/acsami.3c00218
ACS Appl. Mater. Interfaces 2023, 15, 18205−18216

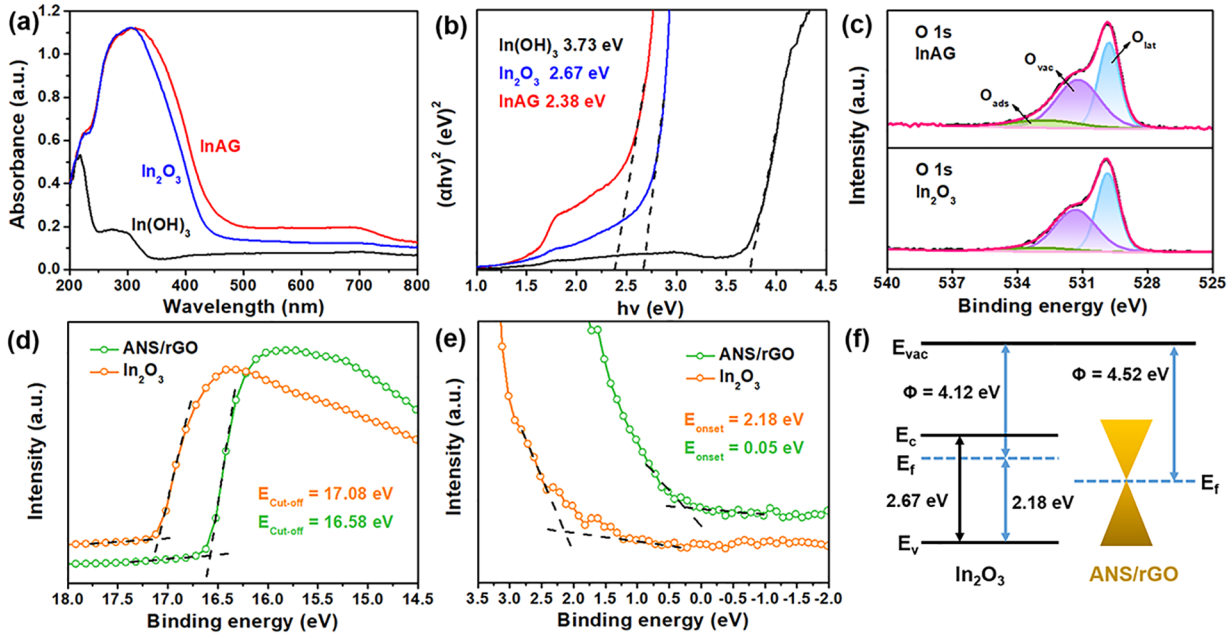

Figure 3. (a) UV−vis DRS and (b) Kubelka−Munk plots of InAG nanohybrids, In_2O_3 nanorods, and $In(OH)_3$. (c) High-resolution O 1s spectra of InAG and In_2O_3 nanorods. (d) Secondary electron emission spectra, (e) valence band spectra, and (f) energy band structure schematics of ANS/rGO and In_2O_3 nanorods.

In_2O_3 formed by the calcination of $In(OH)_3$ exhibit a nanorod-like structure (Figure 2h). Figure S3 shows that the average length and diameter of In_2O_3 are 13.6 and 3.2 nm, respectively, which are less than the Debye length (25 nm[30]) of In_2O_3. Furthermore, the TEM image of InAG nanohybrids (Figure 2i) also clearly demonstrates that the In_2O_3 nanorods are anchored on the wrinkled ANS/rGO nanosheets, which is consistent with the SEM image. In the high-resolution TEM (HRTEM) image of InAG nanohybrids (Figure 2j), the lattice fringes with spacings of 0.292 and 0.413 nm correspond to the (222) and (211) crystal planes of cubic In_2O_3, respectively. The selected area electron diffraction (SAED) pattern in Figure 2k is composed of multiple concentric rings corresponding to the (211), (222), (400), (440), and (622) crystal plans of In_2O_3, separately, revealing the polycrystalline structure of In_2O_3.[31] Figure S4 presents the HAADF STEM image and EDS mapping patterns of InAG nanohybrids, which clearly show the uniform distribution of In, O, C, N, and S elements. The In and O elements are derived from In_2O_3 nanorods, and the C, N, and S elements are derived from rGO and ANS molecules, indicating the successful preparation of InAG nanohybrids.

As shown in Figure 3a, InAG nanohybrids, In_2O_3 nanorods, and $In(OH)_3$ have absorption in the UV region within the range of 200−400 nm, while the absorption of In_2O_3 and InAG in the visible range (400−500 nm) is significantly enhanced. The appearance of the absorption band means that the 400−500 nm photon energy is greater than the band gap of the semiconductor, indicating that electrons in In_2O_3 can transfer from the top of the valence band to the bottom of the conduction band.[32] The band gaps can be estimated by the Kubelka−Munk function formula (see the Supporting Information for details).[33,34] As shown in Figure 3b, the forbidden band widths of $In(OH)_3$, In_2O_3, and InAG are 3.73, 2.67, and 2.38 eV, respectively. According to previous studies,[15,34] the reduction of the band gap of In_2O_3 nanorods after calcination can be attributed to a large amount of oxygen vacancy (O_{vac}) defects. New donor energy levels can be formed by O_{vac} in the band gap of In_2O_3, expanding the light absorption range and improving the separation efficiency of photogenerated electrons and holes.

The EPR approach can identify oxygen vacancies by capturing unpaired electrons in the sample. The *g*-factor provides magnetic information on the material and can be calculated from the resonance conditions (see the Supporting Information for details).[15,33] As presented in Figure S5, InAG exhibits a *g* signal (2.003) at the magnetic field of 3511 G after calcination owing to the presence of singly ionized oxygen vacancies.[35] Figure S6a shows the full XPS spectra of $In(OH)_3$, In_2O_3 nanorods, and InAG. The high-resolution spectrum of In 3d (Figure S6b) shows two peaks at 452.09 and 444.53 eV which are attributed to the spin−orbit splitting of In $3d_{3/2}$ and In $3d_{5/2}$ in In_2O_3, respectively.[18] After assembling with ANS/rGO, the peak position of In 3d shifted slightly toward the lower binding energy owing to the electron transfer and interaction between In_2O_3 and ANS/rGO.[21,23] The high-resolution O 1s spectra of In_2O_3 and InAG (Figure 3c) are fitted to three peaks at 529.86, 531.36, and 533.16 eV, corresponding to lattice oxygen (O_{lat}), oxygen vacancies (O_{vac}), and adsorbed oxygen species (O_{ads}), respectively.[23] The peak position and O_{lat}, O_{vac}, and O_{ads} species relative contents are listed in Table S1. The O 1s spectrum of $In(OH)_3$ is fitted to two peaks at 531.44 and 532.46 eV (Figure S6c), corresponding to In—OH and surface-adsorbed oxygen/water,[36] respectively. In the C 1s spectrum of InAG (Figure S6d), three peaks with binding energies at 284.81, 286.16, and 288.86 eV are assigned to C=C/C—C (sp^2/sp^3 hybridized carbon), C—O (hydroxyl or epoxy carbon), and C=O (carboxyl) groups, respectively.[9,32,37] The N 1s peak at 400.57 eV and the S 2p peak at 167.78 eV can be observed in the spectrum of InAG (Figure S6e,f), proving the successful assembly of ANS/rGO nanosheets and In_2O_3 nanorods.

https://doi.org/10.1021/acsami.3c00218
ACS Appl. Mater. Interfaces 2023, 15, 18205−18216

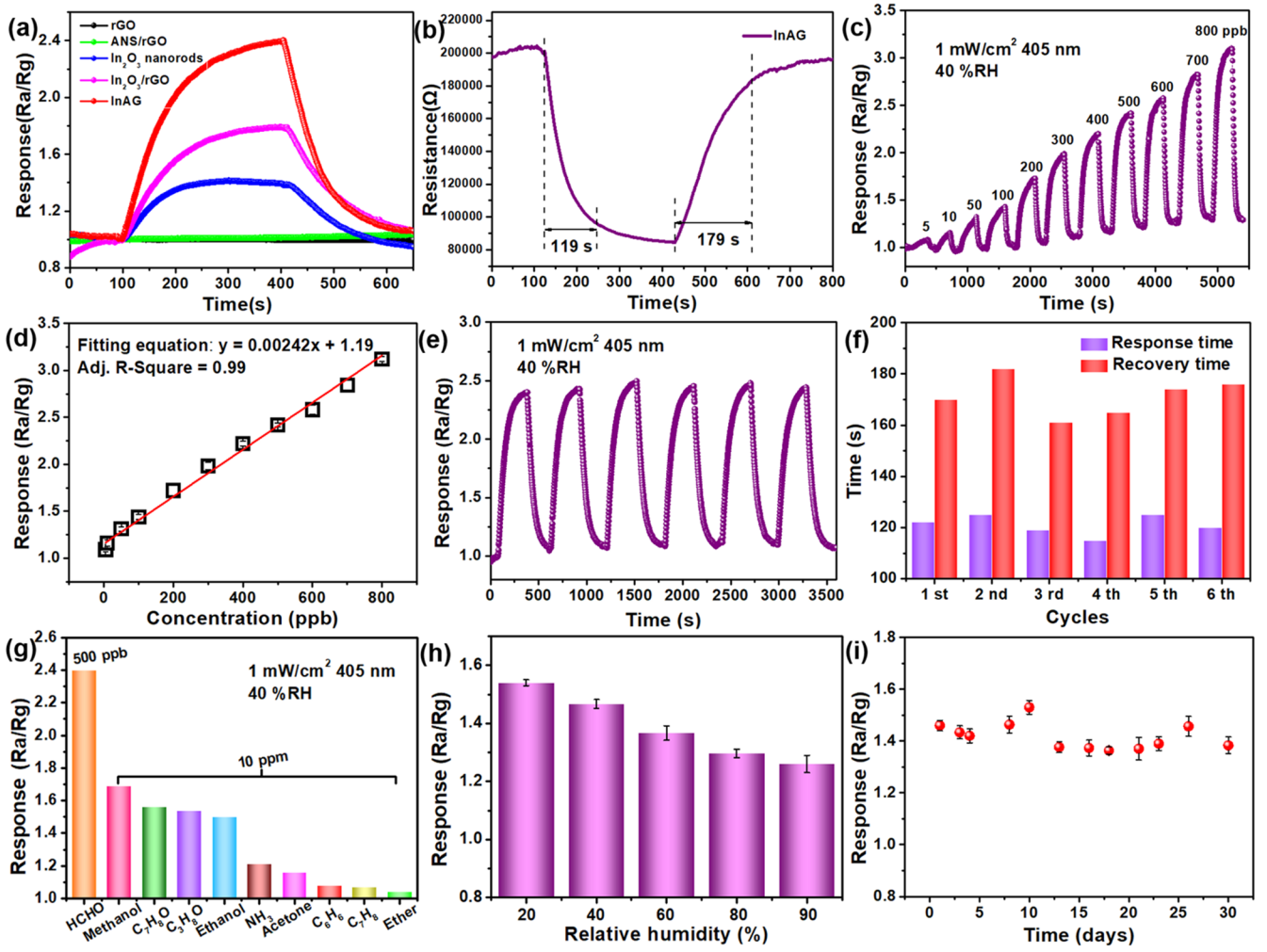

Figure 4. (a) Typical responses of rGO, ANS/rGO, In_2O_3 nanorods, In_2O_3/rGO, and InAG after exposure to 500 ppb HCHO. (b) Response/recovery characteristics of InAG before and after exposure to 500 ppb HCHO at RT. (c) Real-time response curves of the InAG sensor toward different concentrations of HCHO at RT and (d) corresponding linear relationship between concentration and response. (e) Repeatability of InAG nanohybrids toward 500 ppb HCHO at RT and (f) corresponding response/recovery times for each cycle. (g) Selectivity of the InAG sensor toward 500 ppb HCHO and 10 ppm of various interfering gases. (h) Sensor response toward 100 ppb HCHO in the relative humidity range 20−90% RH. (i) Long-term stability of the sensor toward 100 ppb HCHO for up to one month at RT.

UPS was used to confirm the band structure of In_2O_3 and ANS/rGO, as well as the charge transfer between them. The secondary electron emission spectra (Figure 3d) and valence band spectra (Figure 3e) can be obtained from the UPS spectrum of In_2O_3 and ANS/rGO in Figure S7.[38,39] The work functions (Φ) of In_2O_3 and ANS/rGO are calculated to be 4.12 and 4.62 eV. At the composite heterojunction interface, electrons will migrate from In_2O_3 to ANS/rGO. The position of the top of the valence band (E_v) with reference to the Fermi level position (E_f) is extracted from the onset energy of the valence band edge (E_{onset}). The E_{onset} values of In_2O_3 and ANS/rGO are 2.18 and 0.05 eV, respectively (Figure 3e). See the Supporting Information for detailed calculations of Φ and E_v. Based on the calculation results of UPS and UV−vis DRS tests, the schematic diagram of the energy band of In_2O_3 and ANS/rGO is shown in Figure 3f.

Gas-Sensing Performance. Figure S8a displays the current−voltage (I−V) characteristic curves of the nanohybrids under dark and different wavelengths of visible light illumination (1 mW cm^{-2}). The currents of the sensor increase significantly after being exposed to 405 and 460 nm visible light illumination, and the photocurrent decreases with the increase of visible light wavelength. The electrical properties of the InAG-based sensors were further tested under 405 nm illumination with different power densities (Figure S8b). The I−V characteristic curves show that the photoresponse increases with the increase of power density, which can be attributed to the transition of more electrons in the valence band when the power density increases. All I−V currents show a linear increase with increasing voltage, indicating a good Ohmic contact between the sensing materials and Ag/Pd IEDs. Figure S8c shows the effects of darkness and different wavelengths of visible light illumination (1 mW cm^{-2}) on HCHO-sensing properties of the InAG-based gas sensor. The InAG-based sensor exhibits a high response of 2.4 toward 500 ppb HCHO under 405 nm light illumination, which is higher than that under 460 nm light illumination. Nevertheless, it shows no response to the same concentration of HCHO under dark and 530 nm light illumination. The effect of visible light wavelength on gas sensing is related to the energy of the photons. When the photon energy is greater than the band gap of In_2O_3, electrons in the valence band are excited to transition

https://doi.org/10.1021/acsami.3c00218
ACS Appl. Mater. Interfaces 2023, 15, 18205−18216

Table 1. Performance Comparison of RT Formaldehyde Sensors Reported to Date

materials	sensor type[a]	light wavelength	conc.[b] (ppm)	response[c]	t_{res}/t_{rec}	D_R[d] (ppm)
VG/SnO_2[40]	CR	no	5	1.046[B]	46/95 s	0.3−5
$ZnSnO_3/MXene$[41]	CR	no	100	2.94[B]	6.2/5.1 s	5−100
$rGO/N\text{-}MXene/TiO_2$[42]	CR	no	20	2.32[B]	−/−	4−40
$Ni-In_2O_3/WS_2$[43]	CR	no	5	1.3[A]	76/123 s	0.05−20
PDA-GO[44]	CR	no	300	1.24[B]	74/129 s	50−300
$1T/2H\text{-}MoS_2$[45]	FET	no	1	∼1.14[B]	150/330 s	0.1−10
Pd/Au[46]	FET	no	1	1.35[B]	−/−	0.02−0.8
$Pt/Ti_{0.75}Nb_{0.25}N$[47]	PEMFC	no	50	10.42[C]	14/19 s	0.1−50
MOF-ZnO[48]	CR	365 nm (8.31 mW cm^{-2})	100	14.05[A]	6/22 s	0.1−100
POM@ZIF-8@ZnO[49]	CR	Xe lamp (100 mW cm^{-2})	100	5.4[A]	15.1/16.2 s	25−200
$TiO_2@SnO_2$[50]	CR	365 nm (2.5 mW cm^{-2})	10	20[A]	20/56 s	0.1−10
5MMM/TiO_2[51]	CR	365 nm (225 mW)	5	1352[A]	9 s/−	0.025−5
Au-TiO_2[8]	CR	365 nm (2.5 mW cm^{-2})	5	8.5[A]	36/110 s	0.1−10
In_2O_3/PW_{12}[52]	CR	Xe lamp (100 mW cm^{-2})	100	1.82[A]	−/−	5−100
MoS_2/rGO[53]	CR	>420 nm (1.2 mW cm^{-2})	10	1.64[B]	17/98 s	1−50
ZnOx@ANS-rGO[6]	CR	405 nm (2 mW cm^{-2})	1	1.58[A]	47/39 s	0.01−1
In_2O_3/ANS/rGO (this work)	*CR*	*405 nm* (1 mW cm^{-2})	*0.5*	*2.4*[A]	*119/179 s*	*0.005−0.8*

[a]CR, FET, and PEMFC represent chemiresistive, field-effect transistor, and proton exchange membrane fuel cell type gas sensors, respectively. [b]conc.: concentration. [c]For ease of comparison, the evaluation of response is converted as A, response = R_a/R_g; B, response = R_g/R_a; and C, response = $I_g - I_a$ (μA). [d]D_R represents the detection range and is taken from the sensor's real-time response curves for different concentrations of formaldehyde.

to the conduction band to produce photogenerated electron−hole pairs. The photogenerated electrons are captured by adsorbed oxygen to produce reactive oxygen which can react with formaldehyde. The sensing performance of the sensor decreases with the increases of wavelength of visible light because only fewer electrons can be excited by the long wavelength light (low energy wavelength). In view of the above results, 405 nm light illumination was adopted in the following work. The relationship between light power density and HCHO-sensing response was further explored. As shown in Figure S8d, the responses of the InAG-based sensor toward 500 ppb HCHO under 405 nm light illumination have little dependence on the light power density ranging from 0.25 to 3 mW cm^{-2}. The highest response value (R_a/R_g = 2.4) occurs under 1 mW cm^{-2} light power density. Thus, 1 mW cm^{-2} is selected as the optimal light power density.

Figure 4a displays the sensing measurement response curves of rGO, ANS/rGO nanosheets, pristine In_2O_3 nanorods, In_2O_3/rGO, and InAG nanohybrids toward 500 ppb HCHO under 1 mW cm^{-2} 405 nm illumination at RT. The pristine In_2O_3 nanorods, In_2O_3/rGO, and InAG nanohybrids exhibit similar response curves toward HCHO. In contrast, the response of InAG nanohybrids is 1.7 and 1.3 times higher than those of pristine In_2O_3 nanorods and In_2O_3/rGO, respectively. In comparison, the responses of InMAG toward HCHO are significantly lower than that of InAG nanohybrids (Figure S8e), which is attributed to the large area heterojunction of InAG nanohybrids that enhances the sensing capability. In addition, rGO and ANS/rGO nanosheets show no obvious response after being exposed to HCHO. Figure 4b shows the response/recovery resistance curve of the InAG nanohybrid sensor toward 500 ppb HCHO. The resistance of the sensor decreases rapidly after being exposed to HCHO and returns to the initial value after HCHO release, showing n-type semiconductor sensing characteristics. Response/recovery time is an important indicator to evaluate the performance of gas sensors. The response and recovery times of the InAG-based sensor under 405 nm illumination are 119 and 179 s, respectively. Figure 4c shows the gas-sensing properties of nanohybrids exposed to different concentrations of HCHO under 405 nm illumination. The responses of the nanohybrid sensor increase monotonically with the increase of HCHO concentration in the range 5−800 ppb. There is an excellent positive linear relationship between response value and HCHO concentration, with a slope of 0.00242 ppb^{-1} and an R^2 of 0.988 (Figure 4d). Moreover, the sensor shows significant response/recovery characteristics even at a trace concentration of 5 ppb HCHO (Figure 4c). The pLOD is much lower than the HCHO permissible exposure limit of 80 ppb, which has positive significance for the preparation and practical application of trace HCHO sensors. The theoretical LOD of the nanohybrids for HCHO detection is calculated to be 0.13 ppb based on the root-mean-square noise amplitude (rms_{noise}) of the sensor (see the Supporting Information for calculation details). A comparison of the sensing properties of typical room temperature HCHO sensors reported in recent years is summarized in Table 1. It is worth noting that our sensor exhibits a high response (0.5 ppm, R_a/R_g = 2.4) and the lowest pLOD (5 ppb) among the reported HCHO sensors. Excellent sensing properties show a unique competitive advantage in the field of RT formaldehyde sensing.

Figure 4e presents the response/recovery curves of the InAG sensor for 6 cycles toward 500 ppb HCHO under 405 nm illumination. The response values and response/recovery times (Figure 4f) remain stable over 6 cycles, indicating the good repeatability of the sensor. The gas selectivity of InAG nanohybrids was investigated by exposure to 500 ppb HCHO or high concentrations of interfering gases, such as methanol, benzyl alcohol (C_7H_8O), isopropanol (C_3H_8O), ethanol, ammonia (NH_3), acetone, benzene (C_6H_6), toluene (C_7H_8), and ether (Figure 4g). The sensor exhibits outstanding selectivity for HCHO compared to interfering gases, which may be due to the strong adsorption capacity of In_2O_3 for formaldehyde.[5,43] Furthermore, large-area InAG heterojunctions provide an abundance of adsorption sites for HCHO.[54] The O_{vac} defects activate the adsorbed oxygen on

https://doi.org/10.1021/acsami.3c00218
ACS Appl. Mater. Interfaces 2023, 15, 18205−18216

the surface of materials under light illumination, facilitating the adsorption and surface reaction of HCHO.[5,55] The response values of the InAG nanohybrid sensor toward 100 ppb HCHO were measured under different relative humidity (RH) conditions. As shown in Figure 4h, the response decreases gradually as humidity increases from 20% to 90%. Nevertheless, the response of the InAG sensor toward 100 ppb HCHO reaches 1.26 at 90% RH, indicating that the sensor can maintain operation under high humidity conditions. The decrease in response is because the adsorbed water molecules on the surface of sensing materials occupy some active sites, which hinders the adsorption of the supposed oxygen and HCHO molecules.[56] The stability of the InAG nanohybrids sensor toward 100 ppb HCHO over 30 days was further tested. As shown in Figure 4i, the sensor exhibits good long-term stability with a drop in response value of only about 7% within a month.

To verify the practicability and reliability of the fabricated RT sensor in actual environmental pollutant monitoring, a 3 m^3 simulated indoor environmental pollutant test chamber equipped with a temperature and humidity control system and air samplers was used for field detection (Figure 5a). 1.5−8.0

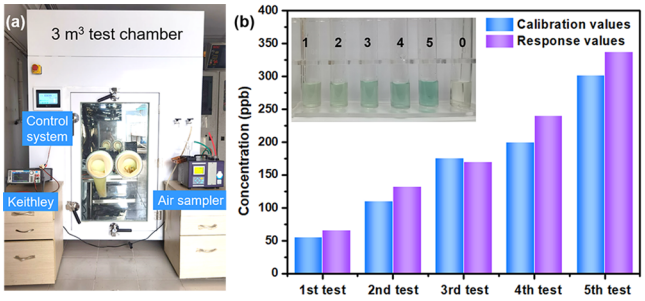

Figure 5. (a) 3 m^3 test chamber equipped with a temperature and humidity control system and air sampler for the simulation of indoor environmental pollutants. (b) Correlation between sensor response values and spectrophotometric calibration values; the inset shows a colorimetric tube with analytical reagents for formaldehyde concentration.

μL formalin solutions were heated and volatilized to formaldehyde gas of different concentrations. The formaldehyde concentrations (calibration values) in the test chamber were accurately calibrated by phenol reagent spectrophotometry[57] (see the Supporting Information for details). The responses of the sensor were brought into the fitting equation (Figure 4d) to obtain the corresponding formaldehyde concentrations (response values). As can be seen from Figure 5b, the response values of the sensor are in excellent agreement with the accurate calibration values, with high accuracy and reliability, and show great practical prospects in pollutant detection.

Formaldehyde-Sensing Mechanism. Here, we propose a mechanism for the enhanced HCHO sensing of InAG nanohybrids under visible light illumination (Figure 6). The improved sensing properties of InAG nanohybrids can be attributed to more interfacial depletion layers coming from large-area heterojunctions and more efficient charge transfer resulting from visible-light radiation. As one of the mainstream gas-sensing mechanism models, the gas adsorption/desorption model is suitable for metal-oxide-based gas sensors.[58] To better understand the HCHO-sensing mechanism of InAG nanohybrids, the sensing mechanism of pristine In_2O_3 is first discussed. The abundant O_{vac} defects in In_2O_3 endow it with visible-light absorption properties. Under 405 nm light illumination, electrons in the valence band gain energy and transition to the conduction band to form photogenerated electron−hole pairs. In fresh air, oxygen molecules (O_2) in the surrounding environment will be adsorbed on the surface of In_2O_3 and capture photogenerated electrons in the conduction band to form active oxygen ions. Among these active oxygen ions (O_2^-, O^-, and O^{2-}), O_2^- is the dominant species.[39,59] In addition, an electron depletion layer (EDL) is formed on the surface of In_2O_3, which is helpful for the increase of initial resistance. When exposed to HCHO, O_2^- on the surface of In_2O_3 oxidizes HCHO molecules to form carbon dioxide (CO_2) and water (H_2O).[55] At the same time, the photogenerated electrons captured by O_2 are released to the conduction band, resulting in the narrowing of the EDL (n-type sensing behavior). The reaction process is shown in eqs 1−4.

$$h\upsilon \rightarrow e^-(h\upsilon) + h^+(h\upsilon) \quad (1)$$

$$O_2(g) \rightarrow O_2(ads) \quad (2)$$

$$O_2(ads) + e^-(h\upsilon) \rightarrow O_2^-(ads) \quad (3)$$

$$O_2^-(ads) + HCHO(g) \rightarrow CO_2 + H_2O + e^- \quad (4)$$

On one hand, the superior sensing properties of the InAG sensor compared to pristine In_2O_3 are attributed to ultrasmall In_2O_3 nanorods and more efficient charge transfer among HCHO molecules, In_2O_3 nanorods, and rGO nanosheets. The diameter and length of In_2O_3 nanorods are less than twice the Debye length of In_2O_3 (25 nm).[30] Therefore, the EDL occupies almost the entire grain, and the potential barrier at the interface formed between In_2O_3 is relatively high. As shown in Figure 6b, when HCHO is introduced to react with O_2^- (ads), the wider EDL is more sensitive to the released electrons, and the potential barrier decreases sharply. The larger change in the potential barrier at the grain boundaries increases the response during the aerodynamic reaction. In addition, organic molecules as surface dopants can effectively modulate the electronic properties of graphene.[60] According to the density functional theory (DFT) calculations,[13] ANS with a donor-π-acceptor (D−π−A) structure acts as a bridge for charge transfer, accelerating the electron transfer among HCHO molecules, In_2O_3 nanorods, and rGO, which promotes the HCHO-sensing properties of InAG.

On the other hand, large-area heterojunctions drive the generation of more interfacial depletion layers, enhancing the HCHO-sensing properties. According to UPS results (Figure 3f), the work function of ANS/rGO (4.52 eV) is larger than that of In_2O_3 (4.12 eV). In InAG nanohybrids, some electrons migrate from In_2O_3 to ANS/rGO, balancing the Fermi level (Figure 6c). According to our previous work, organic-molecule-modified rGO possesses p-type sensing behavior.[12] Furthermore, the modification of ANS prevents the stacking of rGO sheets and increases the contact area between ANS/rGO nanosheets and In_2O_3 nanorods. Compared to the large In_2O_3 microrods, ultrasmall In_2O_3 nanorods have a larger interface contact area with the well-dispersed ANS/rGO nanosheets. Thus, large-area p−n heterojunctions and depletion layers are formed at the interface of ANS/rGO and In_2O_3, and the built-in electric field in the heterojunction leads to band bending at

https://doi.org/10.1021/acsami.3c00218
ACS Appl. Mater. Interfaces 2023, 15, 18205−18216

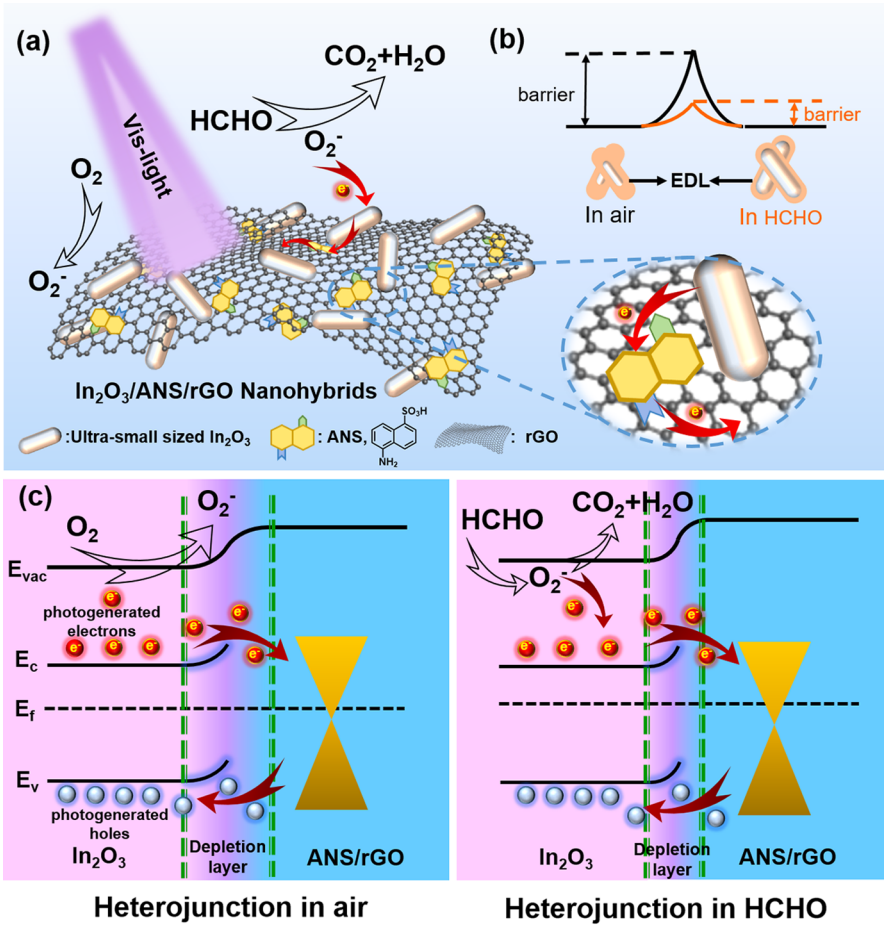

Figure 6. Enhanced sensing mechanism of InAG nanohybrids. (a) Reaction of HCHO molecules on the surface of InAG nanohybrids under 405 nm light illumination. (b) Changes in EDL thickness and potential barrier of In_2O_3 homojunction in air and HCHO. (c) Energy band diagram of InAG heterojunction in air and HCHO atmosphere.

the interface, which effectively improves the separation efficiency of photogenerated carriers. Similar to what is described earlier, the presence of the depletion layer increases the resistance of sensing materials; electrons released significantly increase the conductivity of the InAG sensor when HCHO molecules are present.

CONCLUSION

We presented a VLD heterojunction of InAG which was composed of ultrasmall In_2O_3 nanorods and supramolecularly functionalized rGO nanosheets. The InAG-based sensor exhibited outstanding properties toward low concentrations of HCHO under 405 nm illumination, including high response, relatively short response/recovery times, and reliable repeatability, with the advantage of low power consumption. What is commendable is that the sensor realized the ultralow pLOD of 5 ppb toward HCHO at RT. Sensing mechanism studies demonstrated that the generation of more interfacial depletion layers and the implementation of more efficient charge transfer were jointly responsible for the ultrasensitive room temperature HCHO-sensing properties of InAG. The remarkable practicability and reliability of the InAG sensor in monitoring indoor HCHO pollutants were verified by using a 3 m^3 test chamber. This work provides an effective strategy for the development of ultrasensitive RT ppb-level gas sensors.

EXPERIMENTAL SECTION

Preparation of ANS/rGO Nanosheet Dispersions. Graphene oxide (GO) was prepared from high-purity graphite powder by an improved Hummers' method (for details, see the Supporting Information). An ANS supramolecular functionalized graphene nanosheet dispersion was synthesized as follows. A total of 90 mg of ANS, 4 mL of GO dispersion (1 mg/mL), and 5 mL of NaOH solution (4 mg/mL) were added to 10 mL of deionized water and stirred for 10 min under 80 °C. Then, 10 mL of the hydrazine hydrate solution (1.2 μL/mL) was added dropwise to the above-mixed liquid and stirred for another 1 h. The product was naturally cooled to RT and washed with deionized water by vacuum filtration using a 0.22 μm filter membrane. Subsequently, a homogeneous ANS/rGO nanosheet dispersion was obtained by redispersing the resultant in deionized water. For comparison, rGO was prepared in the same way without adding ANS molecules.

Preparation of In_2O_3 Nanorods. 0.3 g of $In(NO_3)_3{\cdot}xH_2O$ and 0.14 g of hexamethylenetetramine were added into a flask filled with 5 mL of deionized water and stirred at 100 °C for 2 h. After the solution naturally cooled down below 30 °C, the white solid precipitated product was collected by centrifugation, washed thoroughly with deionized water and ethanol several times, and then dried at 60 °C in air. The obtained samples, the precursor of In_2O_3 nanorods, were calcined in a tube furnace at 200, 300, and 400 °C, separately, for 2 h under an argon atmosphere. The gas-sensing results showed that the In_2O_3 calcined at 300 °C had a higher response to formaldehyde (Figure S9a). Hence, all In_2O_3 used in this work were calcined at 300 °C. For comparison, In_2O_3 microrods were prepared using urea instead of hexamethylenetetramine in the synthesis step to verify the

https://doi.org/10.1021/acsami.3c00218
ACS Appl. Mater. Interfaces 2023, 15, 18205−18216

effect of the interface area of the heterojunction formed between In_2O_3 with different sizes and graphene on gas-sensing properties.

Preparation of In_2O_3/ANS/rGO Nanohybrids. 100 mg of In_2O_3 and a certain amount of ANS/rGO dispersion were introduced into 5 mL of deionized water with stirring. The mass ratio of ANS/rGO nanosheets and In_2O_3 were 0.1%, 0.5%, 2.5%, and 12.5%. Then, the mixture was ultrasonicated for 30 min to allow In_2O_3 to evenly adsorb on ANS/rGO nanosheets to obtain assembled In_2O_3/ANS/rGO nanohybrids. The products were collected via centrifugation (10000 rpm) and then dried at 80 °C in air. For comparison, In_2O_3 nanorods/ANS/rGO and In_2O_3 microrods/ANS/rGO were prepared in the same manner. The gas-sensing results (Figure S9b) show that nanohybrids with a mass ratio of 0.5% exhibit a better response to formaldehyde. Here, 0.5% is chosen as the optimal ratio for characterization and sensing tests. For convenience, In_2O_3 nanorods/ANS/rGO and In_2O_3 microrods/ANS/rGO are abbreviated as InAG and InMAG, respectively.

Sensor Fabrication and Performance Measurements. The sensor devices were fabricated using the drip-coating method. Briefly, 2 μL of each sensing material dispersion (100 mg/mL) was uniformly drop-coated on a ceramic substrate with 5 pairs of Ag/Pd interdigitated electrodes (IDEs) and dried at 60 °C in air. The gas-sensing properties of the InAG nanohybrid-based sensor under light illumination were tested by a Keithley 2450 source meter (Tektronix) under an excitation voltage of 0.01 V direct current. The light sources used light-emitting diodes (LED) whose power density can be controlled by an applied voltage and calibrated by a silicon photodiode sensor S120VC (Thorlabs). Dry formaldehyde gas (Dalian Special Gases Co., Ltd.) with a concentration of 50 ppm was selected as the target gas. The gas-sensing measurements were carried out in a homemade sensor test system in ambient air with relative humidity (RH) of 40 ± 5% at RT (25 ± 3 °C). In addition, the applied bias voltage of the sensors during the tests was 0.01 V, showing a low power consumption. In the process of the gas-sensing test, the photocurrent value of nanohybrids reached a stable platform under 405 nm illumination (power density: 1 mW cm^{-2}) first, and then, different volumes of 50 ppm formaldehyde gas were injected into the test chamber (17 L) to reach the desired formaldehyde concentration. For volatile organic compounds (VOCs, including ethanol, acetone, benzene, etc.), the liquids were injected on a heating plate inside the test chamber through a microsyringe and volatilized for detection. The gas response (S) to reducing gases of the sensor devices is defined as $S = R_a/R_g$, where R_a and R_g represent the stable resistance of the sensors in the air and target gas atmosphere, respectively. The response time (t_{res}) and recovery time (t_{rec}) are defined as the times required for 90% of a full response and for a full recovery, respectively.

Materials Characterization. The crystalline structures of the as-obtained samples were characterized by an X-ray diffractometer (XRD, Bruker D8 Advance) with Cu Kα. Fourier transform infrared spectra were obtained by an infrared spectrometer (FTIR, Vertex 70). The Raman spectra were tested by a Raman spectrometer (Raman, Renishaw inVia) with a 532 nm laser source. The ultraviolet−visible diffuse reflectance spectra (DRS) of the samples were measured by a UV−vis spectrophotometer (UV−vis, Shimadzu UV-2600). The morphology and microstructure of the as-prepared samples were observed using field-emission scanning electron microscopy (FE-SEM, ZEISS Gemini 500) and transmission electron microscopy (TEM, JEM-2100HR). Energy dispersive X-ray spectroscopy (EDS) mapping was analyzed by high-angle annular dark-field scanning transmission electron microscopy (HAADF STEM, FEI Talos F200X). Atomic force microscopy (AFM, Multimode8) was used to measure the thickness and profile of rGO and ANS/rGO nanosheets in ScanAsyst mode. X-ray photoelectron spectroscopy (XPS) and ultraviolet photoelectron spectroscopy (UPS) were characterized using a photoelectron spectrometer (Shimadzu AXIS Supra). XPS was used to analyze the surface elemental composition of the samples with a monochromatic Al/Ag dual anode X-ray source, and C 1s at 284.8 eV was used as a reference. UPS was used to measure the work function of the samples with a He I (21.2 eV) UV light source. ζ potentials of the samples were acquired in ultrapure water via dynamic light scattering (Brookhaven NanoBrook Omni). The oxygen vacancy signals were investigated by electron paramagnetic resonance spectrometry (EPR, Bruker EMXPlus-10/12).

■ ASSOCIATED CONTENT

Supporting Information

The Supporting Information is available free of charge at https://pubs.acs.org/doi/10.1021/acsami.3c00218.

Preparation of GO; photographs of GO, rGO, and ANS/rGO aqueous dispersions; additional characterization of the materials with SEM images, HAADF STEM image, EDS mapping patterns, EPR spectrum, XPS spectra, and UPS spectrum; gas-sensing measurements; calculation of band gap, g-factor, work function, energy position of the valence band, rms_{noise}, and theoretical LOD; phenol reagent spectrophotometry details for the calibration of HCHO concentrations (PDF)

■ AUTHOR INFORMATION

Corresponding Author

Yao Wang − *Guangdong Provincial Key Laboratory of Optical Information Materials and Technology, Institute of Electronic Paper Displays, South China Academy of Advanced Optoelectronics, South China Normal University, Guangzhou 510006, P. R. China; National Center for International Research on Green Optoelectronics, South China Normal University, Guangzhou 510006, P. R. China;* orcid.org/0000-0002-0713-5018; Email: wangyao@m.scnu.edu.cn

Authors

Lanpeng Guo − *Guangdong Provincial Key Laboratory of Optical Information Materials and Technology, Institute of Electronic Paper Displays, South China Academy of Advanced Optoelectronics, South China Normal University, Guangzhou 510006, P. R. China; National Center for International Research on Green Optoelectronics, South China Normal University, Guangzhou 510006, P. R. China*

Hongping Liang − *Guangdong Provincial Key Laboratory of Optical Information Materials and Technology, Institute of Electronic Paper Displays, South China Academy of Advanced Optoelectronics, South China Normal University, Guangzhou 510006, P. R. China; National Center for International Research on Green Optoelectronics, South China Normal University, Guangzhou 510006, P. R. China*

Huiyun Hu − *Guangdong Provincial Key Laboratory of Optical Information Materials and Technology, Institute of Electronic Paper Displays, South China Academy of Advanced Optoelectronics, South China Normal University, Guangzhou 510006, P. R. China; National Center for International Research on Green Optoelectronics, South China Normal University, Guangzhou 510006, P. R. China*

Shenbin Shi − *Guangdong Provincial Key Laboratory of Optical Information Materials and Technology, Institute of Electronic Paper Displays, South China Academy of Advanced Optoelectronics, South China Normal University, Guangzhou 510006, P. R. China; National Center for International Research on Green Optoelectronics, South China Normal University, Guangzhou 510006, P. R. China*

Chenxu Wang − *Guangdong Provincial Key Laboratory of Optical Information Materials and Technology, Institute of Electronic Paper Displays, South China Academy of*

https://doi.org/10.1021/acsami.3c00218
ACS Appl. Mater. Interfaces 2023, 15, 18205−18216

Advanced Optoelectronics, South China Normal University, Guangzhou 510006, P. R. China; National Center for International Research on Green Optoelectronics, South China Normal University, Guangzhou 510006, P. R. China

Sitao Lv − *Guangdong Provincial Key Laboratory of Optical Information Materials and Technology, Institute of Electronic Paper Displays, South China Academy of Advanced Optoelectronics, South China Normal University, Guangzhou 510006, P. R. China; National Center for International Research on Green Optoelectronics, South China Normal University, Guangzhou 510006, P. R. China*

Haihong Yang − *Department of Thoracic Oncology, State Key Laboratory of Respiratory Diseases, The First Affiliated Hospital of Guangzhou Medical University, Guangzhou 510006, P. R. China*

Hao Li − *Guangdong Provincial Key Laboratory of Optical Information Materials and Technology, Institute of Electronic Paper Displays, South China Academy of Advanced Optoelectronics, South China Normal University, Guangzhou 510006, P. R. China; National Center for International Research on Green Optoelectronics, South China Normal University, Guangzhou 510006, P. R. China*

Nicolaas Frans de Rooij − *National Center for International Research on Green Optoelectronics, South China Normal University, Guangzhou 510006, P. R. China*

Yi-Kuen Lee − *Department of Mechanical & Aerospace Engineering, Hong Kong University of Science and Technology, Kowloon, Hong Kong Special Administrative Region; Department of Electronic & Computer Engineering, Hong Kong University of Science and Technology, Kowloon, Hong Kong Special Administrative Region*

Paddy J. French − *BE Laboratory, EWI, Delft University of Technology, Delft 2628CD, The Netherlands*

Guofu Zhou − *Guangdong Provincial Key Laboratory of Optical Information Materials and Technology, Institute of Electronic Paper Displays, South China Academy of Advanced Optoelectronics, South China Normal University, Guangzhou 510006, P. R. China; National Center for International Research on Green Optoelectronics, South China Normal University, Guangzhou 510006, P. R. China;* orcid.org/0000-0003-1101-1947

Complete contact information is available at: https://pubs.acs.org/10.1021/acsami.3c00218

Author Contributions

L. Guo: Conceived and designed the research, carried out all laboratory research, wrote draft of manuscript. H. Liang: Discussed the concepts and revised the manuscript. H. Hu, S. Shi, C. Wang, S. Lv: Data collection and visualization. H. Yang, H. Li, N. F. de Rooij, Y.-K. Lee, P. J. French: Helped discuss the data and revise the manuscript. Y. Wang: Oversight and leadership responsibility for the research activity planning and execution, revising the manuscript. G. Zhou: Designed and discussed the concept, and revised the manuscript.

Notes

The authors declare no competing financial interest.

■ ACKNOWLEDGMENTS

This work was supported by the National Natural Science Foundation of China (Grant No. 51973070), Science and Technology Program of Guangzhou (No. 2019050001), Guangdong Basic and Applied Basic Research Foundation (2022A1515010577 and 2021A1515012420), Innovative Team Project of Education Bureau of Guangdong Province (2018KCXTD009), Guangdong Science and Technology Project-International Cooperation (2022A0505050069), Start-up Foundation from SCNU, Guangdong Provincial Key Laboratory of Optical Information Materials and Technology (No. 2017B030301007), MOE International Laboratory for Optical Information Technologies, and the 111 Project, Science and Technology Innovation Strategy Special Foundation of Guangdong (No. pdjh2022b0136).

■ REFERENCES

(1) Kudo, H.; Suzuki, Y.; Gessei, T.; Takahashi, D.; Arakawa, T.; Mitsubayashi, K. Biochemical Gas Sensor (Bio-Sniffer) for Ultrahigh-Sensitive Gaseous Formaldehyde Monitoring. *Biosens. Bioelectron.* **2010**, *26* (2), 854−858. Tran, T. Y.; Younis, S. A.; Heynderickx, P. M.; Kim, K. H. Validation of Two Contrasting Capturing Mechanisms for Gaseous Formaldehyde between Two Different Types of Strong Metal-Organic Framework Adsorbents. *J. Hazard. Mater.* **2022**, *424*, 127459.

(2) Zhang, D.; Mi, Q.; Wang, D.; Li, T. Mxene/Co_3O_4 Composite Based Formaldehyde Sensor Driven by ZnO/Mxene Nanowire Arrays Piezoelectric Nanogenerator. *Sens. Actuat. B Chem.* **2021**, *339*, 129923.

(3) Han, Z.; Qi, Y.; Yang, Z.; Han, H.; Jiang, Y.; Du, W.; Zhang, X.; Zhang, J.; Dai, Z.; Wu, L.; Fletcher, C.; Wang, Z.; Liu, J.; Lu, G.; Wang, F. Recent Advances and Perspectives on Constructing Metal Oxide Semiconductor Gas Sensing Materials for Efficient Formaldehyde Detection. *J. Mater. Chem. C* **2020**, *8* (38), 13169−13188. Ogbeide, O.; Bae, G.; Yu, W.; Morrin, E.; Song, Y.; Song, W.; Li, Y.; Su, B. L.; An, K. S.; Hasan, T. Inkjet-Printed rGO/Binary Metal Oxide Sensor for Predictive Gas Sensing in a Mixed Environment. *Adv. Funct. Mater.* **2022**, *32* (25), 2113348. Zhu, L. Y.; Miao, X. Y.; Ou, L. X.; Mao, L. W.; Yuan, K.; Sun, S.; Devi, A.; Lu, H. L. Heterostructured α-Fe_2O_3@ZnO@ZIF-8 Core-Shell Nanowires for a Highly Selective MEMs-Based Ppb-Level H_2S Gas Sensor System. *Small* **2022**, *18* (50), No. e2204828.

(4) Chizhov, A.; Rumyantseva, M.; Gaskov, A. Light Activation of Nanocrystalline Metal Oxides for Gas Sensing: Principles, Achievements, Challenges. *Nanomater.* **2021**, *11* (4), 892.

(5) Ou, Y.; Zhu, G.; Liu, P.; Jia, Y.; Zhu, L.; Nie, J.; Zhang, S.; Zhang, W.; Gao, J.; Lu, H.; Huang, Y.; Shi, X.; Hojamberdiev, M. Anchoring Platinum Clusters onto Oxygen Vacancy-Modified In_2O_3 for Ultraefficient, Low-Temperature, Highly Sensitive, and Stable Detection of Formaldehyde. *ACS Sens.* **2022**, *7* (4), 1201−1212.

(6) Liang, H.; Guo, L.; Cao, N.; Hu, H.; Li, H.; Frans de Rooij, N.; Umar, A.; Algarni, H.; Wang, Y.; Zhou, G. Practical Room Temperature Formaldehyde Sensing Based on a Combination of Visible-Light Activation and Dipole Modification. *J. Mater. Chem. A* **2021**, *9* (42), 23955−23967.

(7) Majhi, S. M.; Mirzaei, A.; Navale, S.; Kim, H. W.; Kim, S. S. Boosting the Sensing Properties of Resistive-Based Gas Sensors by Irradiation Techniques: A Review. *Nanoscale* **2021**, *13* (9), 4728−4757. Thota, C.; Modigunta, J. K. R.; Reddeppa, M.; Park, Y. H.; Kim, H.; Kang, H.; Kokkiligadda, S.; Lee, S.; Murali, G.; Park, S. Y.; In, I. Light Stimulated Room-Temperature H_2S Gas Sensing Ability of Cl-Doped Carbon Quantum Dots Supported Ag Nanoparticles. *Carbon* **2022**, *196*, 337−346.

(8) Zhang, S.; Zhao, L.; Huang, B.; Li, X. Enhanced Sensing Performance of Au-Decorated TiO_2 Nanospheres with Hollow Structure for Formaldehyde Detection at Room Temperature. *Sens. Actuat. B Chem.* **2022**, *358*, 131465.

(9) Shanmugasundaram, A.; Gundimeda, V.; Hou, T.; Lee, D. W. Realizing Synergy between In_2O_3 Nanocubes and Nitrogen-Doped Reduced Graphene Oxide: An Excellent Nanocomposite for the Selective and Sensitive Detection of Co at Ambient Temperatures. *ACS Appl. Mater. Interfaces* **2017**, *9* (37), 31728−31740.

(10) Feng, Q.; Huang, B.; Li, X. Graphene-Based Heterostructure Composite Sensing Materials for Detection of Nitrogen-Containing Harmful Gases. *Adv. Funct. Mater.* **2021**, *31* (41), 2104058.
(11) Liang, H.; Hu, H.; Wang, J.; Li, H.; de Rooij, N. F.; Zhou, G.; Wang, Y. Graphene-Based Room Temperature Gas Sensing Materials. *Curr. Chin. Sci.* **2021**, *1* (1), 98−114. Wu, J.; Tao, K.; Zhang, J.; Guo, Y.; Miao, J.; Norford, L. K. Chemically Functionalized 3D Graphene Hydrogel for High Performance Gas Sensing. *J. Mater. Chem. A* **2016**, *4* (21), 8130−8140. Gao, Y.; Wang, J.; Feng, Y.; Cao, N.; Li, H.; de Rooij, N. F.; Umar, A.; French, P. J.; Wang, Y.; Zhou, G. Carbon Iron Electron Transport Channels in Porphyrin-Graphene Complex for Ppb-Level Room Temperature NO Gas Sensing. *Small* **2022**, *18* (11), No. e2103259.
(12) Chen, Z.; Wang, J.; Pan, D.; Wang, Y.; Noetzel, R.; Li, H.; Xie, P.; Pei, W.; Umar, A.; Jiang, L.; Li, N.; Frans de Rooij, N.; Zhou, G. Mimicking a Dog's Nose: Scrolling Graphene Nanosheets. *ACS Nano* **2018**, *12* (3), 2521−2530.
(13) Pei, W.; Zhang, T.; Wang, Y.; Chen, Z.; Umar, A.; Li, H.; Guo, W. Enhancement of Charge Transfer between Graphene and Donor-π-Acceptor Molecule for Ultrahigh Sensing Performance. *Nanoscale* **2017**, *9* (42), 16273−16280.
(14) Liu, W. B.; Zeng, J. W.; Gao, Y. X.; Li, H.; de Rooij, N. F.; Umar, A.; Algarni, H.; Wang, Y.; Zhou, G. F. Charge Transfer Driven by Redox Dye Molecules on Graphene Nanosheets for Room-Temperature Gas Sensing. *Nanoscale* **2021**, *13* (44), 18596−18607.
(15) Gu, F.; Li, C.; Han, D.; Wang, Z. Manipulating the Defect Structure (Vo) of In_2O_3 Nanoparticles for Enhancement of Formaldehyde Detection. *ACS Appl. Mater. Interfaces* **2018**, *10* (1), 933−942.
(16) Zhang, S.; Song, P.; Li, J.; Zhang, J.; Yang, Z.; Wang, Q. Facile Approach to Prepare Hierarchical Au-Loaded In_2O_3 Porous Nanocubes and Their Enhanced Sensing Performance Towards Formaldehyde. *Sens. Actuat. B Chem.* **2017**, *241*, 1130−1138.
(17) Wan, Z.; Mao, Q.; Chen, Q. Proton-Dependent Photocatalytic Dehalogenation Activities Caused by Oxygen Vacancies of In_2O_3. *Chem. Eng. J.* **2021**, *403*, 126389.
(18) Gu, F.; Di, M.; Han, D.; Hong, S.; Wang, Z. Atomically Dispersed Au on In_2O_3 Nanosheets for Highly Sensitive and Selective Detection of Formaldehyde. *ACS Sens.* **2020**, *5* (8), 2611−2619.
(19) Jang, J.-S.; Winter, L. R.; Kim, C.; Fortner, J. D.; Elimelech, M. Selective and Sensitive Environmental Gas Sensors Enabled by Membrane Overlayers. *Trends Chem.* **2021**, *3* (7), 547−560.
(20) Gu, F.; Nie, R.; Han, D.; Wang, Z. In_2O_3−Graphene Nanocomposite Based Gas Sensor for Selective Detection of NO_2 at Room Temperature. *Sens. Actuat. B Chem.* **2015**, *219*, 94−99.
(21) Lv, Y. K.; Li, X. J.; Li, Y. Y.; Liu, X.; Yao, H. C.; Li, Z. J. Construction of Organic-Inorganic "Chelate" Adsorption Sites on Metal Oxide Semiconductor for Room Temperature NO_2 Sensing. *J. Hazard. Mater.* **2022**, *432*, 128623.
(22) Lee, S. H.; Galstyan, V.; Ponzoni, A.; Gonzalo-Juan, I.; Riedel, R.; Dourges, M. A.; Nicolas, Y.; Toupance, T. Finely Tuned SnO_2 Nanoparticles for Efficient Detection of Reducing and Oxidizing Gases: The Influence of Alkali Metal Cation on Gas-Sensing Properties. *ACS Appl. Mater. Interfaces* **2018**, *10* (12), 10173−10184.
(23) Devi, P.; Singh, J. P. Visible Light Induced Selective Photocatalytic Reduction of CO_2 to CH_4 on In_2O_3-rGO Nanocomposites. *J. CO2 Util.* **2021**, *43*, 101376.
(24) Jia, X.; Sun, K.; Wang, J.; Shen, C.; Liu, C.-j. Selective Hydrogenation of CO_2 to Methanol over Ni/In_2O_3 Catalyst. *J. Energy Chem.* **2020**, *50*, 409−415.
(25) Kaur, M.; Jain, N.; Sharma, K.; Bhattacharya, S.; Roy, M.; Tyagi, A. K.; Gupta, S. K.; Yakhmi, J. V. Room-Temperature H_2S Gas Sensing at Ppb Level by Single Crystal In_2O_3 Whiskers. *Sens. Actuat. B Chem.* **2008**, *133* (2), 456−461.
(26) Huang, H.; Yue, Z.; Li, G.; Wang, X.; Huang, J.; Du, Y.; Yang, P. Heterostructured Composites Consisting of In_2O_3 Nanorods and Reduced Graphene Oxide with Enhanced Interfacial Electron Transfer and Photocatalytic Performance. *J. Mater. Chem. A* **2014**, *2* (47), 20118−20125.
(27) Liu, J.; Li, S.; Zhang, B.; Wang, Y.; Gao, Y.; Liang, X.; Wang, Y.; Lu, G. Flower-Like In_2O_3 Modified by Reduced Graphene Oxide Sheets Serving as a Highly Sensitive Gas Sensor for Trace NO_2 Detection. *J. Colloid Interface Sci.* **2017**, *504*, 206−213. Hu, H.; Liang, H.; Fan, J.; Guo, L.; Li, H.; de Rooij, N. F.; Umar, A.; Algarni, H.; Wang, Y.; Zhou, G. Assembling Hollow Cactus-Like ZnO Nanorods with Dipole-Modified Graphene Nanosheets for Practical Room-Temperature Formaldehyde Sensing. *ACS Appl. Mater. Interfaces* **2022**, *14* (11), 13186−13195.
(28) Guo, H. L.; Wang, X. F.; Qian, Q. Y.; Wang, F. B.; Xia, X. H. A Green Approach to the Synthesis of Graphene Nanosheets. *ACS Nano* **2009**, *3* (9), 2653−2659.
(29) Pashchanka, M.; Hoffmann, R. C.; Gurlo, A.; Schneider, J. J. Molecular Based, Chimie Douce Approach to 0D and 1D Indium Oxide Nanostructures. Evaluation of Their Sensing Properties Towards CO and H_2. *J. Mater. Chem.* **2010**, *20* (38), 8311.
(30) Kim, S.; Carpenter, P. D.; Jean, R. K.; Chen, H. T.; Zhou, C. W.; Ju, S.; Janes, D. B. Role of Self-Assembled Monolayer Passivation in Electrical Transport Properties and Flicker Noise of Nanowire Transistors. *ACS Nano* **2012**, *6* (8), 7352−7361.
(31) Ma, J.; Fan, H.; Zheng, X.; Wang, H.; Zhao, N.; Zhang, M.; Yadav, A. K.; Wang, W.; Dong, W.; Wang, S. Facile Metal-Organic Frameworks-Templated Fabrication of Hollow Indium Oxide Microstructures for Chlorine Detection at Low Temperature. *J. Hazard. Mater.* **2020**, *387*, 122017.
(32) Liu, J.; Ke, J.; Li, D.; Sun, H.; Liang, P.; Duan, X.; Tian, W.; Tade, M. O.; Liu, S.; Wang, S. Oxygen Vacancies in Shape Controlled Cu_2O/Reduced Graphene Oxide/In_2O_3 Hybrid for Promoted Photocatalytic Water Oxidation and Degradation of Environmental Pollutants. *ACS Appl. Mater. Interfaces* **2017**, *9* (13), 11678−11688.
(33) Du, W.; Si, W.; Wang, F.; Lv, L.; Wu, L.; Wang, Z.; Liu, J.; Liu, W. Creating Oxygen Vacancies on Porous Indium Oxide Nanospheres Via Metallic Aluminum Reduction for Enhanced Nitrogen Dioxide Detection at Low Temperature. *Sens. Actuat. B Chem.* **2020**, *303*, 127221.
(34) Xu, H.; Wang, Y.; Dong, X.; Zheng, N.; Ma, H.; Zhang, X. Fabrication of In_2O_3/In_2S_3 Microsphere Heterostructures for Efficient and Stable Photocatalytic Nitrogen Fixation. *Appl. Catal., B* **2019**, *257*, 117932.
(35) Qi, Y.; Jiang, J.; Liang, X.; Ouyang, S.; Mi, W.; Ning, S.; Zhao, L.; Ye, J. Fabrication of Black In_2O_3 with Dense Oxygen Vacancy through Dual Functional Carbon Doping for Enhancing Photothermal CO_2 Hydrogenation. *Adv. Funct. Mater.* **2021**, *31* (22), 2100908. Yang, J.; Hu, S.; Fang, Y.; Hoang, S.; Li, L.; Yang, W.; Liang, Z.; Wu, J.; Hu, J.; Xiao, W.; Pan, C.; Luo, Z.; Ding, J.; Zhang, L.; Guo, Y. Oxygen Vacancy Promoted O_2 Activation over Perovskite Oxide for Low-Temperature CO Oxidation. *ACS Catal.* **2019**, *9* (11), 9751−9763.
(36) Çepni, E.; Öznülüer Özer, T. Electrochemical Deposition of Indium(Iii) Hydroxide Nanostructures for Novel Battery-Like Capacitive Materials. *J. Energy Storage* **2022**, *45*, 103678.
(37) Xu, P.; Zhao, S.; Wang, T.; Ji, W.; Chen, Z.; Au, C.-T. A Pt/SnO_2/rGO Interface More Capable of Converting Ethanol to CO_2 in Ethanol Electro-Oxidation: A Detailed Experimental/DFT Study. *J. Mater. Chem. A* **2022**, *10* (18), 10150−10161.
(38) Yang, J.; Xiong, S.; Song, J.; Wu, H.; Zeng, Y.; Lu, L.; Shen, K.; Hao, T.; Ma, Z.; Liu, F.; Duan, C.; Fahlman, M.; Bao, Q. Energetics and Energy Loss in 2D Ruddlesden−Popper Perovskite Solar Cells. *Adv. Energy Mater.* **2020**, *10* (23), 2000687.
(39) Eom, T. H.; Cho, S. H.; Suh, J. M.; Kim, T.; Yang, J. W.; Lee, T. H.; Jun, S. E.; Kim, S. J.; Lee, J.; Hong, S. H.; Jang, H. W. Visible Light Driven Ultrasensitive and Selective NO_2 Detection in Tin Oxide Nanoparticles with Sulfur Doping Assisted by L-Cysteine. *Small* **2022**, *18* (12), No. e2106613.
(40) Bo, Z.; Yuan, M.; Mao, S.; Chen, X.; Yan, J.; Cen, K. Decoration of Vertical Graphene with Tin Dioxide Nanoparticles for Highly Sensitive Room Temperature Formaldehyde Sensing. *Sens. Actuat. B Chem.* **2018**, *256*, 1011−1020.

https://doi.org/10.1021/acsami.3c00218
ACS Appl. Mater. Interfaces 2023, 15, 18205−18216

(41) Sima, Z.; Song, P.; Ding, Y.; Lu, Z.; Wang, Q. $ZnSnO_3$ Nanocubes/$Ti_3C_2T_x$ Mxene Composites for Enhanced Formaldehyde Gas Sensing Properties at Room Temperature. *Appl. Surf. Sci.* **2022**, *598*, 153861.
(42) Wang, Y.; Zhou, Y.; Wang, Y. Humidity Activated Ionic-Conduction Formaldehyde Sensing of Reduced Graphene Oxide Decorated Nitrogen-Doped MXene/Titanium Dioxide Composite Film. *Sens. Actuat. B Chem.* **2020**, *323*, 128695.
(43) Zhang, D.; Cao, Y.; Yang, Z.; Wu, J. Nanoheterostructure Construction and DFT Study of Ni-Doped In_2O_3 Nanocubes/WS_2 Hexagon Nanosheets for Formaldehyde Sensing at Room Temperature. *ACS Appl. Mater. Interfaces* **2020**, *12* (10), 11979−11989.
(44) Song, M. G.; Choi, J.; Jeong, H. E.; Song, K.; Jeon, S.; Cha, J.; Baeck, S.-H.; Shim, S. E.; Qian, Y. A Comprehensive Study of Various Amine-Functionalized Graphene Oxides for Room Temperature Formaldehyde Gas Detection: Experimental and Theoretical Approaches. *Appl. Surf. Sci.* **2020**, *529*, 147189.
(45) Zong, B.; Xu, Q.; Li, Q.; Fang, X.; Chen, X.; Liu, C.; Zang, J.; Bo, Z.; Mao, S. Novel Insights into the Unique Intrinsic Sensing Behaviors of 2D Nanomaterials for Volatile Organic Compounds: From Graphene to MoS_2 and Black Phosphorous. *J. Mater. Chem. A* **2021**, *9* (25), 14411−14421.
(46) Liu, C.; Hu, J.; Wu, G.; Cao, J.; Zhang, Z.; Zhang, Y. Carbon Nanotube-Based Field-Effect Transistor-Type Sensor with a Sensing Gate for Ppb-Level Formaldehyde Detection. *ACS Appl. Mater. Interfaces* **2021**, *13* (47), 56309−56319.
(47) Huang, C.; Adimi, S.; Liu, D.; Guo, H.; Thomas, T.; Attfield, J. P.; Ruan, S.; Qu, F.; Yang, M. Mesoporous Titanium Niobium Nitrides Supported Pt Nanoparticles for Highly Selective and Sensitive Formaldehyde Sensing. *J. Mater. Chem. A* **2021**, *9* (35), 19840−19846.
(48) Ling, W.; Zhu, D.; Pu, Y.; Li, H. The Ppb-Level Formaldehyde Detection with UV Excitation for Yolk-Shell MOF-Derived ZnO at Room Temperature. *Sens. Actuat. B Chem.* **2022**, *355*, 131294.
(49) Wang, P.; Zou, X.; Tan, H.; Wu, S.; Jiang, L.; Zhu, G. Ultrathin ZIF-8 Film Containing Polyoxometalate as an Enhancer for Selective Formaldehyde Sensing. *J. Mater. Chem. C* **2018**, *6* (20), 5412−5419.
(50) Zhang, S.; Zhao, L.; Huang, B.; Li, X. UV-Activated Formaldehyde Sensing Properties of Hollow TiO_2@SnO_2 Heterojunctions at Room Temperature. *Sens. Actuat. B Chem.* **2020**, *319*, 128264.
(51) Jo, Y. K.; Jeong, S. Y.; Moon, Y. K.; Jo, Y. M.; Yoon, J. W.; Lee, J. H. Exclusive and Ultrasensitive Detection of Formaldehyde at Room Temperature Using a Flexible and Monolithic Chemiresistive Sensor. *Nat. Commun.* **2021**, *12* (1), 4955.
(52) Tian, J.; Chen, X.; Wang, T.; Pei, W.; Li, F.; Li, D.; Yang, Y.; Dong, X. Modification of Indium Oxide Nanofibers by Polyoxometalate Electron Acceptor Doping for Enhancement of Gas Sensing at Room Temperature. *Sens. Actuat. B Chem.* **2021**, *344*, 130227.
(53) Wang, J.; Deng, H.; Li, X.; Yang, C.; Xia, Y. Visible-Light Photocatalysis Enhanced Room-Temperature Formaldehyde Gas Sensing by MoS_2/rGO Hybrids. *Sens. Actuat. B Chem.* **2020**, *304*, 127317.
(54) Wang, S.; Cao, J.; Cui, W.; Fan, L.; Li, X.; Li, D.; Zhang, T. One-Dimensional Porous Co_3O_4 Rectangular Rods for Enhanced Acetone Gas Sensing Properties. *Sens. Actuat. B Chem.* **2019**, *297*, 126746.
(55) Deng, L.; Ding, X.; Zeng, D.; Tian, S.; Li, H.; Xie, C. Visible-Light Activate Mesoporous WO_3 Sensors with Enhanced Formaldehyde-Sensing Property at Room Temperature. *Sens. Actuat. B Chem.* **2012**, *163* (1), 260−266.
(56) Liu, L.; Li, X.; Dutta, P. K.; Wang, J. Room Temperature Impedance Spectroscopy-Based Sensing of Formaldehyde with Porous TiO_2 under UV Illumination. *Sens. Actuat. B Chem.* **2013**, *185*, 1−9.
(57) *Standard Method for Hygienic Examination of Formaldehyde in Air of Residential Areas - Spectrophotometric Method*; Standard GB/T 16129-1995; Chinese GB Standards: Beijing, 1996.
(58) Ji, H.; Zeng, W.; Li, Y. Gas Sensing Mechanisms of Metal Oxide Semiconductors: A Focus Review. *Nanoscale* **2019**, *11* (47), 22664−22684.
(59) Eom, T. H.; Cho, S. H.; Suh, J. M.; Kim, T.; Lee, T. H.; Jun, S. E.; Yang, J. W.; Lee, J.; Hong, S.-H.; Jang, H. W. Substantially Improved Room Temperature NO_2 Sensing in 2-Dimensional SnS_2 Nanoflowers Enabled by Visible Light Illumination. *J. Mater. Chem. A* **2021**, *9* (18), 11168−11178.
(60) Zhang, X.; Shao, Z.; Zhang, X.; He, Y.; Jie, J. Surface Charge Transfer Doping of Low-Dimensional Nanostructures toward High-Performance Nanodevices. *Adv. Mater.* **2016**, *28* (47), 10409−10442.

https://doi.org/10.1021/acsami.3c00218
ACS Appl. Mater. Interfaces 2023, 15, 18205−18216